# A Technique for End-Effector Force Estimation in Parallelogram Arm Robot using Link-Integrated Load Cells

*[1]Kayode P. Ayodele, [1]Isaac Omolayo, [1]Elisha A. Komolafe, [1]Abimbola M. Jubril,
[2]Paul Obreba, [3]Adebimpe Ogunmodede, [1]Emmanuel Olateju, [2]Oluwaseun Ajayi,
[4]Matthew O. B. Olaogun and [3]Morenikeji A. Komolafe
[1]Department of Electrical & Electronics Engineering, Obafemi Awolowo University, Ile-Ife, Nigeria
[2]Department of Mechanical Engineering, Obafemi Awolowo University, Ile-Ife, Nigeria
[3]Department of Medicine, Obafemi Awolowo University, Ile-Ife, Nigeria
[4]Department of Physiotherapy, University of Medical Sciences, Ondo City, Nigeria
**kayodele@oauife.edu.ng**

Received: 01-MAY-2023; Reviewed: 13-JUN-2023; Accepted: 28-JUN-2023
http://doi.org/10.46792/fuoyejet.v8i2.1035

**ORIGINAL RESEARCH**

**Abstract-** In end effector rehabilitation robots, user effort is usually measured using highly accurate, but expensive, multi-axis force/torque (F/T) sensors. These sensors are not easily available in developing countries. An alternative force sensing method, making use of low-cost load cells mounted on the active links, is presented. In this study, a model of a robot using the proposed sensing technique was developed, with the placement of the load cells justified using kinematic and dynamic analyses. The relationship between the force applied at the end effector, and force experienced by the load cells was determined. Preliminary experimental validation of the ability to estimate end effector force from the link-integrated load cells was carried out using finite element analysis in SolidWorks. Initial evaluation of tracking accuracy resulted in an average root-mean-square error (RMSE) of 0.566. The application of compensators generated from polynomial regressors resulted in over 300% improvement in performance, resulting in an average RMSE of 0.053. The results show that proposed technique can be used to accurately estimate forces at the end effector at relatively low costs.

**Keywords-** Parallelogram Arm Robot; End Effector; Load-Cell; Finite Element Analysis.

## 1 INTRODUCTION

There is growing evidence that robot-assisted therapy (RAT) can help reverse motor function impairments following neurological events such as stroke (Krebs, 2018; Hesse *et al.*, 2006). Many studies have examined the effectiveness of RAT for recovery of leg, arm, and full-body motor function, with the arm receiving the most attention, as it plays a crucial role in performing daily activities (Krebs *et al.*, 2004; Shakti *et al.*, 2018; Abdulkareem *et al.*, 2018). Despite promising results from RAT studies, clinical adoption has been slow, largely due to the perceived high cost of RAT, which can reach hundreds of thousands of dollars (Krebs and Hogan, 2012). There is thus keen interest in developing cost-effective rehabilitation robots.

Other than actuators and drive electronics, force/ torque sensors are often among the most expensive components in rehabilitation robots. This is due to the need to accurately estimate the force of interaction between the robot and its environment (usually a human holding an end effector in the case of end effector robots. This ensures patient safety and facilitates the performance of exercises that promote motor and neural plasticity. Examples of high-quality force-torque sensors include the ATI F/T sensor Axia 130-M125, which was used in the RE-HAROB study (Toth et al., 2004), and other sensors from companies such as Jr3, HBM, and ATI. These sensors can be costly, with products similar to the Axia 130 costing around $6,500 (ATI Industrial Automation, 2023). Rehabilitation robots with a parallelogram arm structure are constitute a major class of planar end-effector rehabilitation robots. These types of robots are much smaller and lighter compared to other planar rehabilitation robots. Unlike other planar robots, the parallelogram arrangement allows patients to move freely within the robot's workspace. Parallelogram arm robots have a structure that consists of two parallel links connected by four revolute joints, forming a parallelogram shape. The end effector, which is typically a hand or gripper, is attached to the end of one of the links and is used to interact with the environment. Sensing typically occurs at the end effector, allowing the robot to measure forces and movements during therapy. Some notable parallelogram rehabilitation robots include the MIT MANUS (Hogan *et al.*, 1992), Casadio *et al.*, (2006), Squeri *et al.*, 2009 and the hybrid rehabilitation robot by Freeman (Freeman *et al.*, 1992).

In this paper, a new technique for estimating end effector force in parallelogram arm robots is presented. We term this technique "sensing via arm-integrated load cells" (SAIL). It involves the integration of low-cost single-axis load cells into some links of a parallelogram arm robot, allowing the force of interaction at the end effector of the robot to be estimated by measuring the forces exerted on the load cells. The design, kinematic, and dynamic analysis of the technique are presented in Section 2 of this paper. Section 3 describes experiments to verify the operation of a SAIL system via finite element analysis within a computer-aided design (CAD)/computer-aided engineering (CAE) software environment. The results of these simulations are presented in Section 4, along with discussions of important observations and implications

* Corresponding Author

**Section B-** ELECTRICAL/COMPUTER ENGINEERING & RELATED SCIENCES
**Can be cited as:**
Ayodele K. P., Omolayo I., Komolafe E.A., Jubril A.M., Obreba P., Ogunmodede A., Olateju E., Ajayi O., Olaogun M.O.B. and Komolafe M.A. (2023). A Technique for End-Effector Force Estimation in Parallelogram Arm Robot using Link-Integrated Load Cells, FUOYE Journal of Engineering and Technology, 8(2), 184-191. http://doi.org/10.46792/fuoyejet.v8i2.1035

## 2 Design and Analysis

### 2.1 Determination of Alternative Sensing Sites

Fig. 1 shows the geometry of a typical parallelogram arm robot configuration on which the SAIL technique is based. Torques are generated by the motors at the resolute joints B, to which link $l_1$ and link $l_2$ are directly coupled. Forces and torques generated by the subject are applied at the end effector at A. The forces and torques from the two ends A and B interact through the four links.

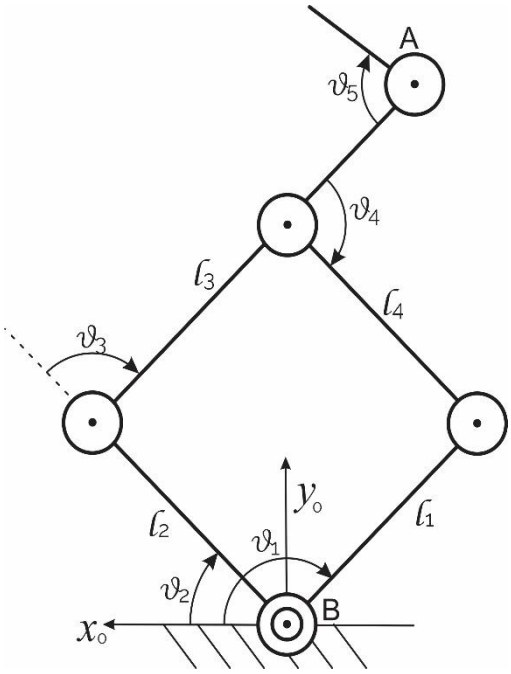


Fig. 1: Geometry of parallelogram arm robot

If sensing is not done at the end effector, it can plausibly be done somewhere on the links, or at B. Energy injected at points A and B induce different patterns of motion and stresses in the rigid arms. Optimal placement of sensors along the links can result in the measurement of these motions and stresses. End effector forces can thereafter be estimated on the bases of such measurements. In determining potential alternative sites at which to sense user effort, the number of degrees of freedom (DOF) is important. This is a 2 DOF system. Consequently, a minimum of two independent variables needs to be monitored to minimize loss of information about end effector force. In addition, energy between points A and B propagate through two paths (through link $l_2$ and link $l_3$, or link $l_1$ and link $l_4$). This motivates a belief that at least one quantity should be measured on each path.

There are slight differences in the motion and stress patterns for the links in Fig. 1. Link $l_1$ and link $l_2$ are constrained at B, and are each capable of 1 DOF motion. The other two links are each capable of 2 DOF of translational motion, and 1 DOF of rotational motion. This affects the patterns of stress vectors in each pair. For the first pair, energy transmission across the link induces only rotational motion, with the links consequently predominantly experiencing flexural stresses. The other two links link $l_3$ and link $l_4$ on the other hand, may experience predominantly compressive, tensile, or flexural stressors at different times. Accordingly, sensing on link $l_3$ and link $l_4$ will necessarily be multivariate (to measure compressive, tensile, and flexural stresses), while sensing of just flexural stress on link $l_1$ and link $l_2$ might provide sufficient information. The foregoing motivated a decision to place a sensing element for flexural stress on each of link $l_1$ and link $l_2$ (as depicted in Fig. 2). This placement also ensures that both independent paths of energy propagation are monitored, while ensuring that the least number of sensors and measurands are utilized.

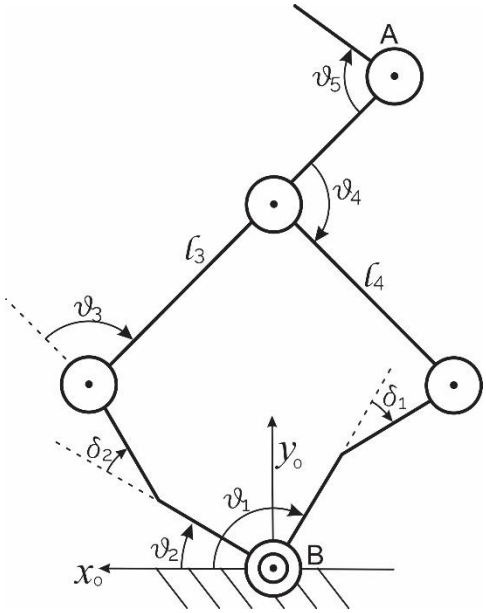


Fig 2: Modified version of parallelogram arm geometry due to insertion of load cells

### 2.2 Kinematics

The insertion of breaks at the midpoints of link $l_1$ and link $l_2$ introduces a number of changes to the geometry. As shown in Fig. 2, the deflections $\delta_1$ and $\delta_2$, caused by the insertions can make the geometry more complicated. However, the deformations experienced by load cells under full load are typically negligible. For example, a 50 kg load cell such as MT1041 load-cell (Mettler Todedo 2007) would be appropriate for the range of force generated by a typical adult arm. This load cell model has a maximum deflection of 0.5 mm along its long axis of length 40 mm. Consequently, $\delta_1$ and $\delta_2$ can be assumed to be negligibly small, allowing analysis of the parallelogram arm with inserted load cells to proceed on the basis of Fig. 1 for now.

From Fig. 3, the position, $\mathbf{A}(x, y)$ of the end effector within the robot workspace can be determined as a function of the angles at the active links $\vartheta_1$ and $\vartheta_2$ as follows:

$$\mathbf{A} = \begin{bmatrix} l_2\cos\vartheta_2 + l_3\cos\vartheta_1 \\ l_2\sin\vartheta_2 + l_3\sin\vartheta_1 \end{bmatrix} \quad [1]$$



http://doi.org/10.46792/fuoyejet.v8i2.1035 http://journal.engineering.fuoye.edu.ng/

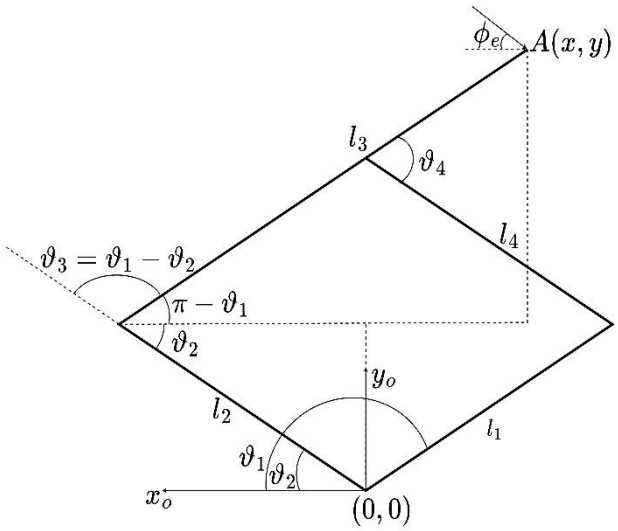


Fig. 3: Kinematic analysis of parallelogram arm

### 2.3 Dynamic Analysis

The generalized dynamic model for a manipulator with a vector of joint angles given by $\mathbf{q} = [\vartheta_1 \quad \vartheta_2]^T$ is:

$$\mathbf{B(q)\ddot{q} + C(q,\dot{q})\dot{q} + F\dot{q} + g(q) = \tau - J^T(q)F_e} \qquad [2]$$

where: $\mathbf{B}$ = Inertia matrix of the manipulator
$\mathbf{C}$ = Coriolis terms
$\mathbf{F}$ = Frictional terms
$\mathbf{g}$ = Gravitational terms
$\boldsymbol{\tau}$ = Motor torque
$\mathbf{J}$ = Jacobian matrix
$\mathbf{F_e}$ = Force at end effector.

Parallelogram arm rehabilitation robots are usually oriented to use a horizontal plane of motion. That orientation is assumed in this study, resulting in the elimination of the gravity component of Eq. 2. For actuation, they usually use brushless direct current or stepper motors with rated speeds of between a few thousand rpm and possibly as high as 100,000 rpm. These speeds are too high for direct coupling to the links. Coupled with the fact that higher torque motors are usually bulkier and more expensive, a more economic approach involves coupling a gearbox to the motors. This increases torque, reduces speeds, but also increases the impedance. Increased impedance can be useful when performing rehabilitation tasks, as it allows patients to undergo resistance training, and with use of appropriate control, the device can be experimentally tuned to mimic a wider range of different loads to subjects.

The following development will assume that either due to the use of gearboxes or otherwise, the impedance of the motor at rest is high enough that it requires significant effort by the user to set it into motion. Before the user has applied enough force to move the revolute joints, all links can be considered stationary. This implies a system at static equilibrium, for which $\dot{\mathbf{q}} = 0$, leading to a reduction of Eq. 2 to:

$$\mathbf{T = J^T F_e} \qquad [3]$$

where $\mathbf{J}$, the Jacobian, is:

$$\mathbf{J} = \begin{pmatrix} \frac{\delta x}{\delta \vartheta_1} & \frac{\delta x}{\delta \vartheta_2} \\ \frac{\delta y}{\delta \vartheta_1} & \frac{\delta y}{\delta \vartheta_2} \end{pmatrix} = \begin{pmatrix} -l_3 \sin\vartheta_1 & -l_2 \sin\vartheta_2 \\ l_3 \cos\vartheta_1 & l_2 \cos\vartheta_2 \end{pmatrix} \qquad [4]$$

The torque, $\mathbf{T}$ in Eq. 3, is the vector of torques induced at joint B (Fig. 1) due to the force, $\mathbf{F_e}$, applied at the end effector by the user. Due to the high impedance of the motors, the links do not initially rotate. This absence of rotation makes the applied force cause a bending moment on the load cell in the actuated links causing a slight deflection. The force readings $\mathbf{F_L}$ due to this deflection is as a result of the reactive torque at the active joints which opposes the induced torque. Thus, varying the applied force varies the induced torque which in turn varies the deflection and force readings from the load cell. Hence, a relationship can be inferred between forces measured by the load cells $\mathbf{F_L}$ and induced torque $\mathbf{T}$ as follows:

$$\mathbf{T = k^T F_L} \qquad [5]$$

where: $\mathbf{k}$ is a $2 \times 1$ matrix of constants that can be determined experimentally. The individual torques can then be calculated to be:

$$\begin{pmatrix} T_1 \\ T_2 \end{pmatrix} = \begin{pmatrix} -l_3 \sin\vartheta_1 & l_3 \cos\vartheta_1 \\ -l_2 \sin\vartheta_2 & l_2 \cos\vartheta_2 \end{pmatrix} \begin{pmatrix} F_e \cos\phi_e \\ F_e \sin\phi_e \end{pmatrix} \qquad [6]$$

or,

$$\begin{aligned} T_1 &= -l_3 F_e \cos\phi_e \sin\vartheta_1 + l_3 F_e \sin\phi_e \cos\vartheta_1 \\ T_2 &= -l_2 F_e \cos\phi_e \sin\vartheta_2 + l_2 F_e \sin\phi_e \cos\vartheta_2 \end{aligned} \qquad [7]$$

From Eq. 3,

$$\begin{pmatrix} F_{ex} \\ F_{ey} \end{pmatrix} = (J^T)^{-1} \begin{pmatrix} T_1 \\ T_2 \end{pmatrix} \qquad [8]$$

And from Eq. 4:

$$\begin{aligned} |J^T| &= -l_2 l_3 \sin\vartheta_1 \cos\vartheta_2 + l_2 l_3 \cos\vartheta_1 \sin\vartheta_2 \\ &= -l_2 l_3 \sin(\vartheta_1 - \vartheta_2) \end{aligned} \qquad [9]$$

$$(J^T)^{-1} = -\frac{1}{l_2 l_3 \sin(\vartheta_1 - \vartheta_2)} \begin{pmatrix} l_2 \cos\vartheta_2 & l_2 \sin\vartheta_2 \\ -l_3 \cos\vartheta_1 & -l_3 \sin\vartheta_1 \end{pmatrix} \qquad [10]$$

Therefore:

$$\begin{pmatrix} F_{ex} \\ F_{ey} \end{pmatrix} = -\frac{1}{l_2 l_3 \sin(\vartheta_1 - \vartheta_2)} \times \begin{pmatrix} l_2 \cos\vartheta_2 & l_2 \sin\vartheta_2 \\ -l_3 \cos\vartheta_1 & -l_3 \sin\vartheta_1 \end{pmatrix} \begin{pmatrix} T_1 \\ T_2 \end{pmatrix} \qquad [11]$$

On substituting Eq. 5, this gives:

$$\begin{aligned} F_{ex} &= \frac{-k_1 F_{L1} \cos\vartheta_2 - k_2 F_{L2} \sin\vartheta_2}{l_3 \sin(\vartheta_1 - \vartheta_2)} \\ F_{ey} &= \frac{k_1 F_{L1} \cos\vartheta_1 + k_2 F_{L2} \sin\vartheta_1}{l_2 \sin(\vartheta_1 - \vartheta_2)} \end{aligned} \qquad [12]$$

Expressing this in polar form,

$$\mathbf{F_e} = \frac{\sqrt{\begin{matrix} l_2^2((k_1 F_{L1})^2 \cos\vartheta_2{}^2 + (k_2 F_{L2})^2 \sin\vartheta_2{}^2) + \\ k_1 k_2 F_{L1} F_{L2} (l_2^2 \sin 2\vartheta_2 + l_3^2 \sin 2\vartheta_1 + \\ l_3^2((k_2 F_{L2})^2 \sin\vartheta_1{}^2 + (k_1 F_{L1})^2 \cos\vartheta_1{}^2) \end{matrix}}}{l_2 l_3 \sin(\vartheta_1 - \vartheta_2)} \qquad [13]$$
$$\angle \arctan\left(-\frac{l_3 k_1 F_{L1} \cos\vartheta_1 + l_3 k_2 F_{L2} \sin\vartheta_1}{l_2 k_1 F_{L1} \cos\vartheta_2 + l_2 k_2 F_{L2} \sin\vartheta_2}\right)$$



http://doi.org/10.46792/fuoyejet.v8i2.1035 http://journal.engineering.fuoye.edu.ng/

## 3 Finite Element Analysis

### 3.1 Load Cell Placement

The placement of load cells was based on a prediction about the nature of stress patterns on each of the 4 links as end effector force is applied at different angles. To confirm this prediction, finite element analyses (Asafa, 2019) on the basis of the kinematic structure in Fig. 3 were conducted in the Dassault Systemes SolidWorks CAD software, version 2020. Realistic dimensions were used for all components. The global mesh size was set to 1 mm. A force of 10 N was applied to the end effector in the direction of $x_0$ (Fig. 3). The angle $\phi$ was thereafter varied between 0 and 360 in steps of 45. The simulation was run for each angle, and a plot of Von Mises stresses was obtained. Automation of the large number of simulations was achieved using a C# application developed in Microsoft Visual Studio 2022 Community, interacting with the model through the SolidWorks API.

Table 1. Dimensions and masses of model elements

| Part Name | Length (cm) | Thickness (cm) | Mass (g) |
|---|---|---|---|
| End effector link | 2.1e+11 | N/m$^2$ | |
| Unbroken link | 0.28 | N/A | |
| Broken link (x4) | 7.9e+10 | N/m$^2$ | |
| Load cells strain gauge | 7800 | kg/m$^3$ | |

### 3.2 Sensing Accuracy

The usefulness of the entire SAIL sensing technique depends on the accuracy with which end effector force can be estimated by load cell output. Consequently, the relationship between applied end effector force and load cell output was evaluated. The model in Section 3.1 was modified with the introduction of a load cell model. For realism, a load cell model conforming to the dimensions of the Mettler 1041 load cell was used. A gap of 40 mm was introduced between the faces of the broken links to allow for sufficient deflection of the strain gauge element. Global mesh size remained 1 mm, with a tolerance of 0.05 mm. Additional dimensions and masses are presented in Table 1. The material selected for all the parts of the robot assembly except the load cells was plain carbon steel with properties shown in Table 2, while the load cell material was 7075-T6 aluminium (Table 3). Although the specific aluminium alloy utilized by the Mettler 1041 is not disclosed in publicly available documentation, the 7075-T6 is commonly used for similar applications, hence the choice.

Displacement sensors were placed on the faces of the load cells within the SolidWorks simulation environment, to detect the minute displacement of the load cell when end effector forces were applied. The angles $\vartheta_1$ set to 15 while $\vartheta_2$ held at 0. A force of 10 N was applied at the end effector, with the angle of application, $\phi$, varied between 0 and 360 in steps of 15. This procedure was repeated for values of $\vartheta_1$ between 15 and 120, in steps of 15, resulting in a total of 192 simulations. Load cell displacements at the tip farthest from Point B were recorded for each simulation. The use of load cell deflection as a surrogate variable for load cell output voltage is justified due to the linear relationship between deflection and output voltage. The above procedure was repeated in order to investigate the relationship between end effector force and the displacement of the load cell on Link $l_2$. For these 192 simulations, $\vartheta_1$ was set to 120 while $\vartheta_2$ was varied between 0 and 105 in steps of 15. The magnitude and angles of applied force were as in the first 192 simulations.

Table 2. Properties of carbon steel used for the links

| Property | Value | Unit |
|---|---|---|
| Elastic Modulus | 2.1e+11 | N/m$^2$ |
| Poisson's Ratio | 0.28 | N/A |
| Shear Modulus | 7.9e+10 | N/m$^2$ |
| Mass Density | 7800 | kg/m$^3$ |
| Tensile Strength | 399826000 | N/m$^2$ |
| Yield Strength | 220594000 | N/m$^2$ |
| Thermal Expansion Coefficient | 1.3e-05 | /K |
| Thermal Conductivity | 43 | W/(m·K) |
| Specific Heat | 440 | J/(kg·K) |

## 3 Results and Discussion

Fig. 4 shows the results of the investigation of stress patterns due to a force of 10 N applied at the end effector, with the angle of application, $\phi$ (following the geometry in Fig. 3) varying from 0 to 360$^o$ in steps of 45$^o$. As predicted in Section 2.1, there are differences in the patterns of stress tensors across the links. As expected, link $l_1$ and link $l_2$, constrained as they are to only rotational motion at point B, always experienced flexural stress, as evidenced by the fact that the different stress regions were always parallel to the longest axes on these links in Fig. 4.

Table 3. Properties of 7075-T6 aluminium used in load cell models

| Property | Value | Unit |
|---|---|---|
| Elastic Modulus | 7.2e+10 | N/m$^2$ |
| Poisson's Ratio | 0.33 | N/A |
| Shear Modulus | 2.69e+10 | N/m$^2$ |
| Mass Density | 2810 | kg/m$^3$ |
| Tensile Strength | 570000000 | N/m$^2$ |
| Yield Strength | 505000000 | N/m$^2$ |
| Thermal Expansion Coefficient | 2.3e-05 | /K |
| Thermal Conductivity | 130 | W/(m·K) |
| Specific Heat | 960 | J/(kg·K) |

The stress patterns on the two other links depended on the relative angle between the end effector force direction, and the long axes of the links. Consequently, link $l_3$ experienced mainly flexural stress in Figs. 4b and 4f, but also experienced significant compressive stresses in Figs. 5a, 5g and 5h and tensile stresses in Figs. 5c, 5d, and 5e. Link $l_4$ also experienced flexural, compressive or tensile stresses, depending on the angle between the link and the applied end effector force.

This validates the argument in Section 2.1 on the placement of the sensing elements. Were sensing to be done on link $l_3$ or link $l_4$, the sensor would need to



http://doi.org/10.46792/fuoyejet.v8i2.1035 http://journal.engineering.fuoye.edu.ng/

measure flexural, tensile, and compressive stress. In contrast, using the adopted arrangement whereby a single load cell each was placed on link $l_1$ or link $l_2$, allowed adequately estimate the flexural stresses experienced by the links. The results of the eight sets of simulations to determine measured load cell force in response to constant applied end effector force as $\vartheta_1$ was varied from 15° to 120 ° are shown in Fig. 5a. Fig. 5b shows the corresponding charts for eight values of $\vartheta_2$. The estimated torque ($T_S$) curves for each octet of graphs have been pre-multiplied by arbitrary constants (740 for Fig. 5a and 528 for Fig. 5b) to make comparison to the values predicted by Eq. 7 easier. Although the shapes of the response curves were generally as expected, amplitude and phase variations are evident.

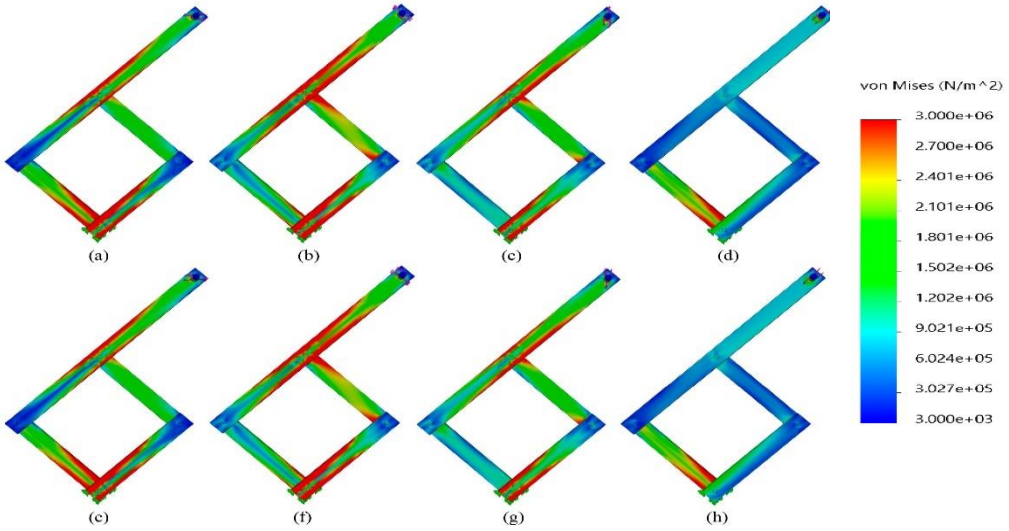


Fig. 4: Stress patterns induced on links by the application of 10 N end effector force at angles (a) 0° (b) 45 ° (c) 90 ° (d) 135 ° (e) 180 ° (f) 225 ° (g) 270 ° (h) 315 °

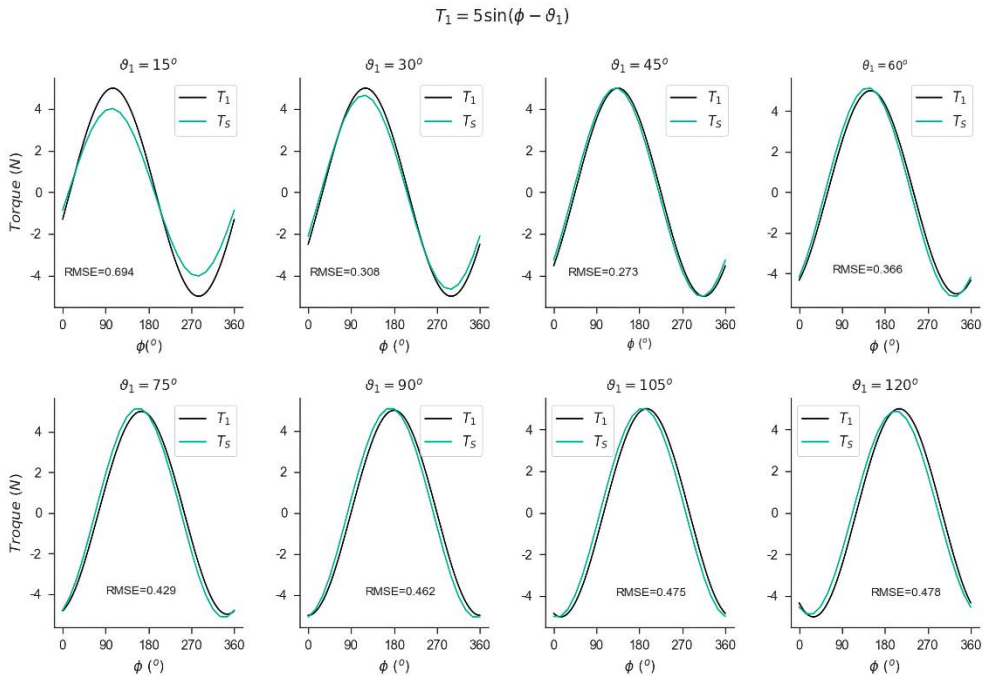


(a)



http://doi.org/10.46792/fuoyejet.v8i2.1035 http://journal.engineering.fuoye.edu.ng/

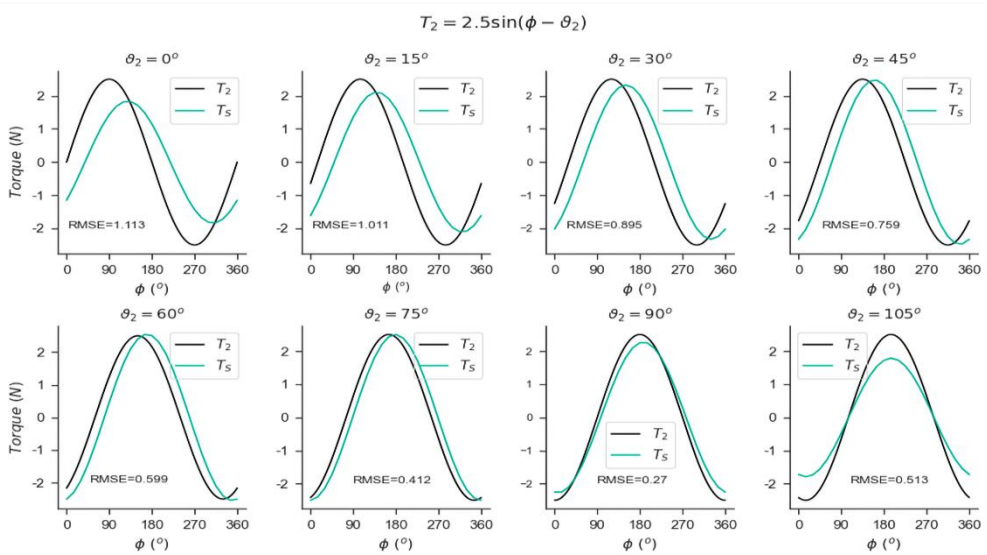


(b)

Fig. 5: Predicted ($T_1$, $T_2$) and experimentally-obtained ($T_S$) relationship between torque and end effector force angle at different link angles for (a) Link $l_1$ (b) Link $l_2$

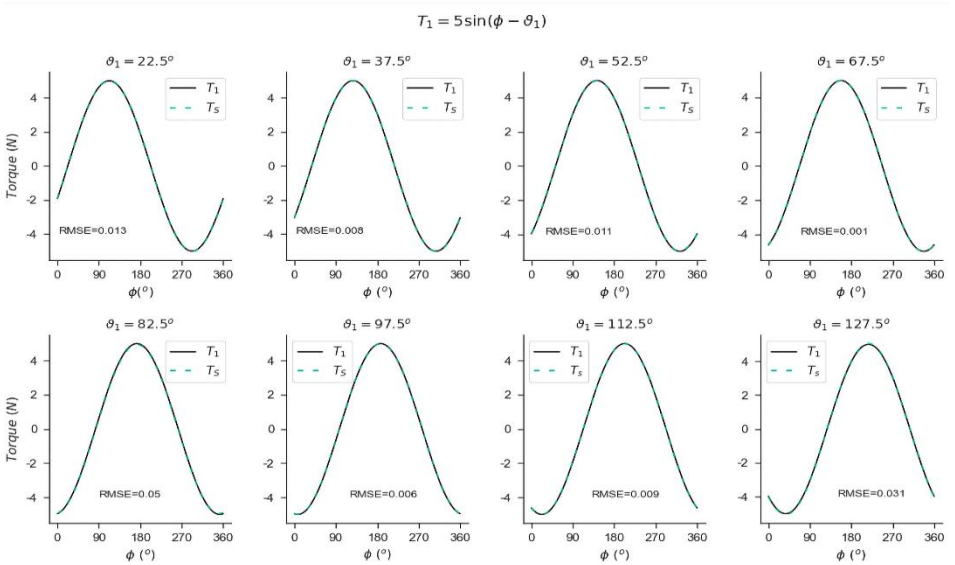


(a)

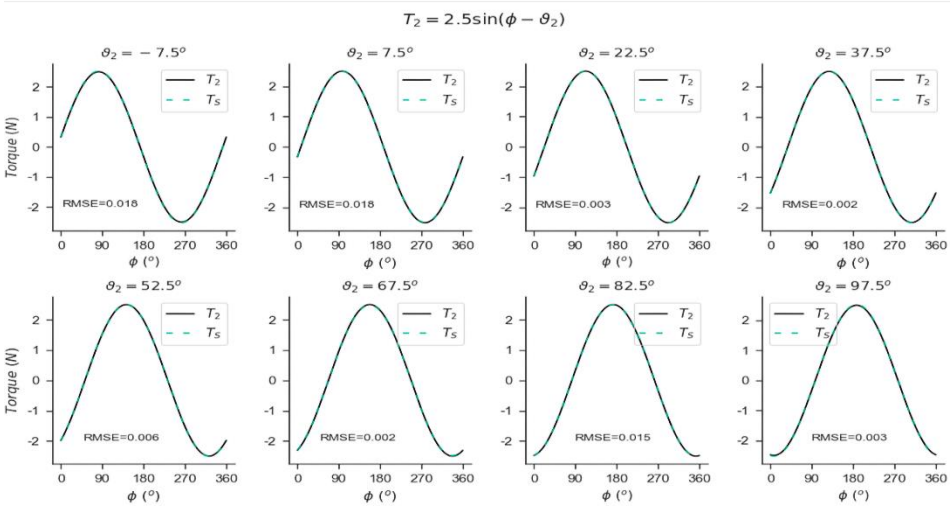


(b)



http://doi.org/10.46792/fuoyejet.v8i2.1035 http://journal.engineering.fuoye.edu.ng/

Fig. 6: Predicted ($T_1$, $T_2$) and experimentally-obtained ($T_S$) relationship between torque and end effector force angle at different link angles after correcting with compensator for (a) Link $l_1$ (b) Link $l_2$

The observed variations are likely due to the slight alterations of overall geometry, as mentioned in the discussion around Fig. 2. An error-correcting compensator was used to account for the deviations. In determining the characteristics of the compensator, it is important to note that the deviations vary with the angle of separation, $\Delta = \vartheta_1 - \vartheta_2$, between the links, rather than the angle of each individual link with the $x_0$ direction. Using the tables of predicted and experimentally obtained values of torque from the data used for Fig. 5, the desired amplitude and phase characteristics of the compensator at different values of $\Delta$ were determined, as presented in Table 4.

Table 4. Frequency responses of load-cell compensators

| $\Delta$() | Load Cell 1 | | Load Cell 2 | |
|---|---|---|---|---|
| | Amplitude | Phase () | Amplitude | Phase () |
| 15 | 919.458 | 2.732 | 738.823 | -0.544 |
| 30 | 794.013 | 3.205 | 581.111 | -7.413 |
| 45 | 738.765 | 4.420 | 528.106 | -13.673 |
| 60 | 719.756 | 5.708 | 518.304 | -19.569 |
| 75 | 717.343 | 6.733 | 532.760 | -25.124 |
| 90 | 723.682 | 7.432 | 567.779 | -30.322 |
| 105 | 737.743 | 7.838 | 626.322 | -34.924 |
| 120 | 756.504 | 7.876 | 718.258 | -38.826 |

Polynomial regressors were fit onto each column of the Table 4, with the minimum polynomial order resulting in an adjusted $R^2 > 0.999$ selected. This allowed the determination of the following correction regressors for the amplitude ($A_1$) and phase ($P_1$) for load cell 1 and load cell 2 ($A_2$ and $P_2$) respectively:

$$A_1 = 6.836e-06\Delta^4 - 0.002404\Delta^3 + 0.325\Delta^2 - 19.43\Delta + 1145$$

$$P_1 = 1.33e-07\Delta^4 - 4.438e-05\Delta^3 + 0.004638\Delta^2 - 0.1106\Delta + 3.479$$

$$A_2 = 1.262e-05\Delta^4 - 0.003925\Delta^3 + 0.4893\Delta^2 - 26.68\Delta + 1040$$

$$P_2 = 0.0009928\Delta^2 - 0.4999\Delta + 6.749$$

The effect of these compensators on the accuracy of end effector sensing was tested by repeating simulation in Section 3.2, this time, with $\vartheta_1$ stepped from 22.5° to 127.5° with $\vartheta_2$ kept constant at 0°, and thereafter, $\vartheta_1$ kept constant at 120° while $\vartheta_2$ was stepped between -7.5° and 97.5°. Correction was effected with compensator with no pre-scaling, resulting in the results shown in Fig. 6. The average root-mean-square error (RMSE) in accurately sensing $T_1$ reduced to 0.016 from 0.436, while the estimation of $T_2$ was now associated with an average RMSE of 0.09 rather than 0.696. This shows that the measurement accuracy was significantly improved by the use of the compensator.

The SAIL technique offers a trade-off between an order-of-magnitude reduction in cost and a slight reduction in accuracy. Such a trade-off might admittedly be unacceptable for industrial applications where attainment of highest possible tracking accuracy is critical, but is likely to be more suitable in rehabilitation robotics applications. Although tracking accuracy provides extremely effective way of quantifying patient improvement, and monitoring the force of interaction between patient and robot, there is no clear evidence that the tracking accuracy itself is the major factor in motor function improvement.

There is no previous report in the literature of a system like this in which end effector force is estimated using end effectors embedded in links. Hence, the primary contribution of this paper is the introduction of the concept, and initial evaluation. Further work needs to be done to quantify the accuracy of the real-life accuracy of the SAIL sensing technique, its suitability for rehabilitation robotics applications, as well as other scenarios in which its use would be recommended. The potential significant reduction in the cost of end effector sensing in rehabilitation robots, and possible domino effect on the viability of rehabilitation robots in resource-constrained environments justify such an endeavour.

## 4 Conclusion

This study was carried out to develop a more cost-effective technique for estimating end-effector force in parallelogram arm robots by integration of low-cost single-axis load cells into some links of a parallelogram. This goal was realized by first carrying out a kinematic analysis of the parallelogram arm to predict the optimal mounting sites of the load cells. A dynamic analysis was also carried out to mathematically show the distribution of torques across the links of the robot. To further confirm the placements of the load cells as predicted from the kinematic analysis, a finite element analysis was carried out. Overall, the results from the above analysis show that the proposed method of sensing via arm integrated load cells is a viable method for measuring applied forces at the end-effector of parallelogram upper limb rehabilitation robots, and whose use can lead to a faster adoption, particularly in developing countries. This study has also left room for additional studies that could lead to more improvements on certain assumptions made during the course of the analyses.

## Acknowledgement

This research was funded by the TETFund National Research Fund 2019. The Nvidia Quadro RTX 8000 GPUs in the workstation were donated by NVidia Corporation.

## References

AbdulKareem, A. H., Adila, A. S., & Husi, G. (2018). Recent trends in robotic systems for upper-limb stroke recovery: A low-cost hand and wrist rehabilitation device. In 2018 2nd international



http://doi.org/10.46792/fuoyejet.v8i2.1035 http://journal.engineering.fuoye.edu.ng/

symposium on small-scale intelligent manufacturing systems (sims) (pp. 1-6). IEEE. DOI:10.1109/SIMS.2018. 8355302

ATI Industrial Automation (2023, January 1). F/T Sensor: Omega160. Https://www.Ati-Ia.com. Retrieved January 12, 2023, from https://www.ati-ia.com/products/ft/ft_models.aspx?id=Omega160

Asafa, T. B. (2019). Studies on the Residual Stress and Strain Gradients in Poly-SiGe Nanocantilevers. FUOYE Journal of Engineering and Technology, 4(1). DOI: https://doi.org/10.46792/fuoyejet.v4i1.303

Casadio, M., Sanguineti, V., Morasso, P. G., and Arrichiello, V., (2006), "Braccio di Ferro: A new haptic workstation for neuromotor rehabilitation" Technology and Health Care, 14(3), pp. 123–142. DOI: 10.3233/THC-2006-14301

Freeman, C. T., Hughes, A. M., Burridge, J. H., Chappell, P. H., Lewin, P. L., & Rogers, E. (2009). A robotic workstation for stroke rehabilitation of the upper extremity using FES. Medical engineering & physics, 31(3), 364-373. DOI: 10.1016/j.medengphy.2008.05.008

Hesse, S., Schmidt, H., & Werner, C. (2006). Machines to support motor rehabilitation after stroke: 10 years of experience in Berlin. Journal of Rehabilitation Research & Development, 43(5). DOI: 10.1682/jrrd.2005.02.0052

Hogan, N., Krebs, H. I., Charnnarong, J., Srikrishna, P., & Sharon, A. (1992). MIT-MANUS: a workstation for manual therapy and training. I. In [1992] Proceedings IEEE International Workshop on Robot and Human Communication (pp. 161-165). IEEE.DOI: 10.1109/ROMAN.1992.253895

Krebs, H. I. (2018). Twenty+ years of robotics for upper-extremity rehabilitation following a stroke. In Rehabilitation Robotics (pp. 175-192). Academic Press. DOI:10.1016/B978-0-12-811995-2.00013-8

Krebs, H. I., & Hogan, N. (2012). Robotic therapy: the tipping point. American journal of physical medicine & rehabilitation/Association of Academic Physiatrists, 91(11 0 3), S290. DOI: 10.1097/PHM.0b013e31826bcd80

Krebs, H. I., Ferraro, M., Buerger, S. P., Newbery, M. J., Makiyama, A., Sandmann, M., ... & Hogan, N. (2004). Rehabilitation robotics: pilot trial of a spatial extension for MIT-Manus. Journal of neuroengineering and rehabilitation, 1(1), 1-15. DOI: 10.1186/1743-0003-1-5

METTLER TOLEDO (2007, July 1). MT1041 Load Cell. Https://www.mt.com. Retrieved January 12, 2023, from https://www.mt.com/mt_ext_files/Editorial/Generic/6/MT1041_LoadCell_Datasheet_Editorial-Generic_1159450025774_files/DataSheet_MT1041_en_0707.pdf

Mises, R. V. (1913). Mechanik der festen Körper im plastisch-deformablen Zustand. Nachrichten von der Gesellschaft der Wissenschaften zu Göttingen, Mathematisch-Physikalische Klasse, 1913, 582-592.

Shakti, D., Mathew, L., Kumar, N., & Kataria, C. (2018). Effectiveness of robo-assisted lower limb rehabilitation for spastic patients: A systematic review. Biosensors and Bioelectronics, 117, 403-415. DOI: 10.1016/j.bios.2018.06.027

Squeri, V., Casadio, M., Vergaro, E., Giannoni, P., Morasso, P., & Sanguineti, V. (2009). Bilateral robot therapy based on haptics and reinforcement learning: Feasibility study of a new concept for treatment of patients after stroke. Journal of rehabilitation medicine, 41(12), 961-965.DOI: 10.2340/16501977-0400

Toth, A., Arz, G., Fazekas, G., Bratanov, D., & Zlatov, N. (2004). 25 Post stroke shoulder-elbow physiotherapy with industrial robots. Advances in Rehabilitation Robotics: Human-friendly Technologies on Movement Assistance and Restoration for People with Disabilities, 391-411. DOI:10.1007/10946978_25